materials

MDPI

Article

A Phase-Field Model for In-Space Manufacturing of Binary Alloys

Manoj Ghosh [1], Muhannad Hendy [2], Jonathan Raush [3] and Kasra Momeni [2,*]

[1] Department of Mechanical Engineering, Michigan State University, East Lansing, MI 48824, USA
[2] Department of Mechanical Engineering, University of Alabama, Tuscaloosa, Al 35487, USA
[3] Department of Mechanical Engineering, The University of Louisiana at Lafayette, Lafayette, LA 70503, USA
* Correspondence: kmomeni@ua.edu

Abstract: The integrity of the final printed components is mostly dictated by the adhesion between the particles and phases that form upon solidification, which is a major problem in printing metallic parts using available In-Space Manufacturing (ISM) technologies based on the Fused Deposition Modeling (FDM) methodology. Understanding the melting/solidification process helps increase particle adherence and allows to produce components with greater mechanical integrity. We developed a phase-field model of solidification for binary alloys. The phase-field approach is unique in capturing the microstructure with computationally tractable costs. The developed phase-field model of solidification of binary alloys satisfies the stability conditions at all temperatures. The suggested model is tuned for Ni-Cu alloy feedstocks. We derived the Ginzburg-Landau equations governing the phase transformation kinetics and solved them analytically for the dilute solution. We calculated the concentration profile as a function of interface velocity for a one-dimensional steady-state diffuse interface neglecting elasticity and obtained the partition coefficient, k, as a function of interface velocity. Numerical simulations for the diluted solution are used to study the interface velocity as a function of undercooling for the classic sharp interface model, partitionless solidification, and thin interface.

Keywords: additive manufacturing; phase transformation; diffuse interphase; partitionless solidification

Citation: Ghosh, M.; Hendy, M.; Raush, J.; Momeni, K. A Phase-Field Model for In-Space Manufacturing of Binary Alloys. *Materials* **2023**, *16*, 383. https://doi.org/10.3390/ma16010383

Academic Editors: Animesh Kumar Basak, Alokesh Pramanik and Chander Prakash

Received: 29 November 2022
Revised: 14 December 2022
Accepted: 22 December 2022
Published: 31 December 2022

1. Introduction

The further away from Earth, the more difficult it will be to transport all the supplies and redundant parts the astronauts may require. As a result, a strong ISM capability for sophisticated and lightweight materials is a must for such missions. NASA has successfully printed polymer parts on the International Space Station (ISS) using the Fused Deposition Modeling (FDM) technology. However, metallic component printing techniques for ISM are still in development [1]. Microgravity ISM cannot be made using typical powder-based additive manufacturing processes. The FDM process is the most promising technology for ISM printing of metallic parts. Printing objects with high integrity, which is directly related to the creation of surface melt for loosely packed metallic powders, is a significant technological difficulty associated with FDM.

The requirement for new high-fidelity analytical and computational tools to predict the process-microstructure-property correlation is one of the critical challenges in the reliable manufacturing of metallic parts utilizing additive manufacturing techniques. The phase-field approach is a powerful and versatile tool for simulating microstructure evolution at the mesoscale, and it has recently become a popular method for studying various microstructure evolutions. Internal variables called order parameters are used to describe the form and distribution of grains in microstructure. These order parameters remain constant within the grains. The narrow region, where the order parameters change among adjacent grains, is known as the interface. The change in order parameters gives the

time-dependent evolution of the microstructure. Reduction in bulk free energy, interfacial energy, and elastic energy are some of the driving forces for microstructure evolution.

In the phase-field method framework, generally, two continuum equations, known as the Cahn-Hilliard nonlinear diffusion equation [2,3] and the Allen-Cahn equation [4], describe the microstructure evolution. The WBM (Wheeler, Boettinger, and McFadden) phase-field model has also been introduced, which deals with the isothermal solidification of a binary alloy. In this model, free energy functional and field equations were developed for the two types of order parameters, i.e., conserved and nonconserved [5]. The WBM model considered both local and gradient free energy and was used to study the impact of solute trapping during rapid solidification [6]. A phase-field model for rapid solidification of the binary alloys that recovers sharp interface solution has also been developed exhibiting solute trapping by asymptotic analysis [7], which later was expanded to non-isothermal solidification of binary alloys [8,9]. Phase-field simulations for dendrite growth coupled with heat and solute diffusion have been presented for a thin interface [10,11], which is valid for unequal solutal diffusivities in the solid and liquid.

Hyperspherical phase-field models for rapid solidification neglecting the surface energy inhomogeneities have recently been developed for diffusionless processes neglecting elasticity [12], with elasticity [13–15], and with elasticity and surface tension [16] that satisfy all stability conditions for a three-phase system. Multiphase-field models have been developed and utilized to study the microstructure of printed Inconel 718 alloy [17] and solute trapping behavior during rapid solidification [18].

Coupled non-equilibrium phase-field and finite element thermal models are used to investigate the microstructure evolution during laser powder bed fusion of Ni-Nb alloy [19]. To predict the solidification structure during the rapid solidification processes, both interface kinetics and thermal diffusion need to be considered [20]. Finite- [21] and thin-interface [22] phase-field models have been developed to study highly non-equilibrium solidification processes and solute trapping during additive manufacturing. A dilute binary alloy phase-field model [23] has also been developed that maps onto the sharp interface continuous growth model [24] for various kinetic effects like solute trapping and solute drag to study the microstructure maps of rapid solidification. The phase-field model was combined with thermal and solutal diffusion as well as solute trapping effect to predict the microstructure for rapid solidification of dilute binary alloy. Phase-field models can also be used to investigate the sensitivity of the final manufactured parts to the variation in manufacturing conditions [25,26]. Recent progress in the development of phase-field models capturing the microstructure of printed parts is reviewed in Refs. [27–32].

In this study, we develop a phase-field potential for binary alloys that satisfies the stability conditions at all temperatures by capitalizing on our models for diffusionless melting/solidification [12,15,33] and materials growth [34,35]. We analytically solved the governing equations for dilute solution approximation and calculated interface velocity as a function of undercooling. We also derived the phase-field model for the thin interface limit and investigated the solute trapping for different interface velocities. Furthermore, we studied the effect of diffusivity and nonlocal energy on the equilibrium composition and the interface velocity. The proposed model, although limited to binary alloys and processes involving near-equilibrium thermodynamics, such as the fused deposition modeling, provide the basis for the development of more advanced models taking into account complex alloys and additive manufacturing processes involving far from equilibrium processes.

2. Phase-Field Model

The phase-field approach can predict the microstructure evolution using a set of internal conserved and nonconserved field variables, continuous along with the interface. These variables control the total free energy of the inhomogeneous microstructure system. To minimize the system's total energy, following the second law of thermodynamics and assuming a linear relationship between the rate of change of order parameters and thermodynamic driving forces, we derive the Ginzburg-Landau (GL) kinetic equations

governing the evolution of microstructure. The Helmholtz free energy of the system can be defined as,

$$\psi = \psi^l + \psi^\nabla = \psi^\theta + \breve{\psi}^\theta + \psi^\nabla, \tag{1}$$

Here, ψ^l is the local free energy and ψ^∇ is the gradient energy. The local free energy is expressed as the sum of thermal energy ψ^θ and the chemical double-well potential energy $\breve{\psi}^\theta$,

$$\psi^\theta(\theta, c, Y) = G_0^\theta + \Delta G_{S0}^\theta(\theta, c) q(Y, a), \tag{2}$$

$$\breve{\psi}^\theta(\theta, c, Y) = A^{S0}(\theta, c)\breve{q}(Y). \tag{3}$$

Here G_0^θ, $\Delta G_{S0}^\theta(\theta, c)$ and $A^{S0}(\theta, c)$ are functions of temperature θ and concentration c, the order parameter, Y changed from 0 to 1 from liquid to solid side, G_0^θ is the free energy of the liquid phase, $f^L(c_L)$, and $\Delta G_{S0}^\theta(\theta, c) = f^S(c_S) - f^L(c_L)$ is the free energy difference between solid and liquid. $f^L(c_L)$ and $f^S(c_S)$ are the free energy densities of liquid and solid as functions of composition, and $A^{S0}(\theta, c)$ is the height of the double-well potential. $q(Y, a)$ and $\breve{q}(Y)$ are connecting functions,

$$q(Y, a) = aY^2 - 2(a-2)Y^3 + (a-3)Y^4, \tag{4}$$

$$\breve{q}(Y) = Y^2(1-Y)^2. \tag{5}$$

Here, a is a material free parameter. The mole fraction c is expressed as,

$$c = \left(c_S^B - c_L^B\right) q(Y, a) + c_L^B, \tag{6}$$

where, c_S^B and c_L^B are the compositions of bulk solid and liquid phases, respectively. From Equations (2) and (3), local free energy is

$$\psi^l = \psi^\theta + \breve{\psi}^\theta = f(c, Y, \theta) = G_0^\theta + \Delta G_{S0}^\theta(\theta, c) q(Y, a) + A^{S0}(\theta, c)\breve{q}(Y). \tag{7}$$

We consider the first derivative of solid and liquid free energies with respect to their concentration to be equal, i.e.,

$$f_{c_S}^S[c_S(x,t)] = f_{c_L}^L[c_L(x,t)]. \tag{8}$$

Here, subscripts indicate derivatives. So, $f_{c_S}^S[c_S(x,t)] = df^S/dc_S$ and $f_{c_L}^L[c_L(x,t)] = df^L/dc_L$. Differentiating Equation (8) with respect to c_S and rearranging,

$$\left(\frac{\partial c_L}{\partial c_S}\right) = \frac{f_{cc}^S(c_S)}{f_{cc}^L(c_L)}, \tag{9}$$

where we used the notations of $f_{cc}^L(c_L) = d^2f^L/dc_L^2$ and $f_{cc}^S(c_L) = d^2f^S/dc_S^2$. Differentiating Equation (6) with respect to c_L, composition of liquid at the interface,

$$\frac{\partial c}{\partial c_L} = q(Y, a)\left(\frac{\partial c_S}{\partial c_L} - 1\right) + 1. \tag{10}$$

Putting values from Equation (9),

$$\frac{\partial c}{\partial c_L} = q(Y, a)\left(\frac{f_{cc}^L(c_L)}{f_{cc}^S(c_S)} - 1\right) + 1. \tag{11}$$

Rearranging Equation (11),

$$\frac{\partial c_L}{\partial c} = \frac{f_{cc}^S(c_S)}{[1 - q(Y, a)]f_{cc}^S(c_S) + q(Y, a)f_{cc}^L(c_L)}. \tag{12}$$

Similarly, for the solid side,

$$\frac{\partial c_S}{\partial c} = \frac{f_{cc}^L(c_L)}{[1-q(Y,a)]f_{cc}^S(c_S) + q(Y,a)f_{cc}^L(c_L)}. \tag{13}$$

Here, c_S is the composition of solid at the interface. Differentiating Equation (6) with respect to Y,

$$\frac{\partial c}{\partial Y} = \left(c_S^B - c_L^B\right)q'(Y,a). \tag{14}$$

Now applying chain rule and Putting value from Equations (12) and (14),

$$\frac{\partial c_L}{\partial Y} = \frac{\left(c_S^B - c_L^B\right)q'(Y,a)f_{cc}^S(c_S)}{[1-q(Y,a)]f_{cc}^S(c_S) + q(Y,a)f_{cc}^L(c_L)}, \tag{15}$$

Similarly, for the solid side,

$$\frac{\partial c_S}{\partial Y} = \frac{\left(c_S^B - c_L^B\right)q'(Y,a)f_{cc}^L(c_L)}{[1-q(Y,a)]f_{cc}^S(c_S) + q(Y,a)f_{cc}^L(c_L)}. \tag{16}$$

The local free energy is

$$\psi^l = G_0^\theta + \Delta G_{S0}^\theta(\theta,c)q(Y,a) + A^{S0}(\theta,c)\breve{q}(Y). \tag{17}$$

Differentiating with respect to Y,

$$\psi^l{}_Y = \frac{\partial}{\partial Y}\left(G_0^\theta\right) + q'(Y,a)\Delta G_{S0}^\theta(\theta,c) + q(Y,a)\frac{\partial}{\partial Y}\left[\Delta G_{S0}^\theta(\theta,c)\right] + A^{S0}(\theta,c)\breve{q}'(Y) + \breve{q}(Y)\frac{\partial A^{S0}(\theta,c)}{\partial Y}. \tag{18}$$

Substituting from Equations (15) and (16),

$$\frac{\partial}{\partial Y}\left[\Delta G_{S0}^\theta(\theta,c)\right] = \frac{\partial}{\partial Y}\left[f^S(c_S) - f^L(c_L)\right] = \frac{\partial}{\partial Y}\left[f^S(c_S)\right] - \frac{\partial}{\partial Y}\left[f^L(c_L)\right] \quad = \left(\frac{\partial f^S(c_S)}{\partial c_S}\right)\frac{\partial c_S}{\partial Y} - \left(\frac{\partial f^L(c_L)}{\partial c_L}\right)\frac{\partial c_L}{\partial Y},$$

$$\Rightarrow \frac{\partial}{\partial Y}\left[\Delta G_{S0}^\theta(\theta,c)\right] = \frac{q'(Y,a)\frac{\partial f^L(c_L)}{\partial c_L}\left(c_S^B - c_L^B\right)\left[f_{cc}^L(c_L) - f_{cc}^S(c_S)\right]}{[1-q(Y,a)]f_{cc}^S(c_S) + q(Y,a)f_{cc}^L(c_L)}.$$

For $\frac{\partial}{\partial Y}\left(G_0^\theta(c_{L)}\right)$ we have,

$$\frac{\partial}{\partial Y}\left(G_0^\theta(c_L)\right) = \frac{\partial}{\partial Y}\left(f^L(c_L)\right) = \left(\frac{\partial f^L(c_L)}{\partial c_L}\right)\frac{\partial c_L}{\partial Y}$$
$$= \frac{\partial f^L(c_L)}{\partial c_L}\frac{\left(c_S^B - c_L^B\right)q'(Y,a)f_{cc}^S(c_S)}{[1-q(Y,a)]f_{cc}^S(c_S) + q(Y,a)f_{cc}^L(c_L)}.$$

Now putting the values of $\frac{\partial}{\partial Y}\left[\Delta G_{S0}^\theta(\theta,c)\right]$ and $\frac{\partial}{\partial Y}\left(G_0^\theta\right)$ in Equation (18),

$$\begin{aligned}\psi_Y^l = {} & q'(Y,a)\Delta G_{S0}^\theta(\theta,c) + \frac{\partial f^L(c_L)}{\partial c_L}\frac{\left(c_S^B - c_L^B\right)q'(Y,a)f_{cc}^S(c_S)}{[1-q(Y,a)]f_{cc}^S(c_S) + q(Y,a)f_{cc}^L(c_L)} \\ & + q(Y,a)\left[\frac{q'(Y,a)\frac{\partial f^L(c_L)}{\partial c_L}\left(c_S^B - c_L^B\right)\left[f_{cc}^S(c_S) - f_{cc}^L(c_L)\right]}{[1-q(Y,a)]f_{cc}^S(c_S) + q(Y,a)f_{cc}^L(c_L)}\right] \\ & + A^{S0}(\theta,c)\breve{q}'(Y) + \breve{q}(Y)\frac{\partial A^{S0}(\theta,c)}{\partial c}\frac{\partial c}{\partial Y} \\ \Rightarrow \psi^l{}_Y = {} & q'(Y,a)\left[\Delta G_{S0}^\theta(\theta,c) + \frac{\partial f^L(c_L)}{\partial c_L}\left(c_S^B - c_L^B\right)\right] + A^{S0}(\theta,c)\breve{q}'(Y) \\ & + \breve{q}(Y)\frac{\partial A^{S0}(\theta,c)}{\partial c}\left(c_S^B - c_L^B\right)q'(Y,a)\end{aligned} \tag{19}$$

Assuming a second-degree gradient energy term, which is the lowest degree potential function granting a linear relation between the thermodynamic driving force and ∇Y, we have [36],

$$\psi^{\nabla} = 0.5\left(\beta^{S0}\nabla Y^2\right) \tag{20}$$

Here, β^{S0} is the gradient energy coefficient. Now, differentiating Equation (20) with respect to Y,

$$\psi^{\nabla}{}_{Y} = \nabla.\left[\beta^{S0}\nabla Y\right]. \tag{21}$$

Substituting the value of free energy and gradient energy in Equation (1),

$$\psi = G_0^{\theta} + \Delta G_{S0}^{\theta}(\theta, c)q(Y, a) + A^{S0}(\theta, c)\breve{q}(Y) + 0.5\left(\beta^{S0}\nabla Y^2\right), \tag{22}$$

and differentiating with respect to Y,

$$\begin{aligned}\psi_Y = q'(Y, a)\left[\Delta G_{S0}^{\theta}(\theta, c) + \frac{\partial f^L(c_L)}{\partial c_L}\left(c_S^B - c_L^B\right)\right] + A^{S0}(\theta, c)\breve{q}'(Y)\\ +\breve{q}(Y)\frac{\partial A^{S0}(\theta, c)}{\partial c}\left(c_S^B - c_L^B\right)\breve{q}'(Y) + \nabla.\left[\beta^{S0}\nabla Y\right].\end{aligned} \tag{23}$$

The GL equation becomes

$$\frac{1}{L_Y}\frac{\partial Y}{\partial t} = -\frac{\partial \psi^l}{\partial Y} + \nabla.\left[\beta^{S0}\nabla Y\right]. \tag{24}$$

Here, L_Y is the kinetic coefficient. For simplicity, we assume $A^{S0}(\theta, c)$ to be independent of c, i.e., $\partial A^{S0}(\theta, c)/\partial c = 0$. Using Equation (19), we have

$$\begin{aligned}\frac{1}{L_Y}\frac{\partial Y}{\partial t} = -\left\{q'(Y, a)\left[\Delta G_{S0}^{\theta}(\theta, c) + \frac{\partial f^L(c_L)}{\partial c_L}\left(c_S^B - c_L^B\right)\right] + A^{S0}(\theta, c)\breve{q}'(Y)\right\}\\ +\nabla.\left[\beta^{S0}\nabla Y\right].\end{aligned} \tag{25}$$

Differentiating Equation (17) with respect to c,

$$\begin{aligned}\psi^l{}_c = q(Y, a)\left(\frac{d}{dc}\left[\Delta G_{S0}^{\theta}(\theta, c)\right]\right) + \frac{\partial}{\partial c}\left(G_0^{\theta}\right) + \breve{q}(Y)\frac{dA^{S0}(\theta, c)}{dc}\\ = q(Y, a)\left[\frac{d}{dc}\left[f^S(c_S)\right] - \frac{d}{dc}\left[f^L(c_L)\right]\right] + \frac{d}{dc}\left[f^L(c_L)\right] + \breve{q}(Y)\frac{dA^{S0}(\theta, c)}{dc}\\ = q(Y, a)\left[\left(\frac{\partial f^S(c_S)}{\partial c_L}\right)\frac{\partial c_S}{\partial c} - \left(\frac{\partial f^L(c_L)}{\partial c_L}\right)\frac{\partial c_L}{\partial c}\right] + \left(\frac{\partial f^L(c_L)}{\partial c_L}\right)\frac{\partial c_L}{\partial c} + \breve{q}(Y)\frac{dA^{S0}(\theta, c)}{dc}\\ = \left(\frac{\partial f^L(c_L)}{\partial c_L}\right)\left[q(Y, a)\left(\frac{\partial c_S}{\partial c} - \frac{\partial c_L}{\partial c}\right) + \frac{\partial c_L}{\partial c}\right] + \breve{q}(Y)\frac{dA^{S0}(\theta, c)}{dc}.\end{aligned} \tag{26}$$

Substituting values from Equations (12) and (13),

$$\psi^l{}_c = \frac{\partial f^L(c_L)}{\partial c_L} + \breve{q}(Y)\frac{dA^{S0}(\theta, c)}{dc}. \tag{27}$$

Differentiating Equation (26) with respect to c considering, $\frac{\partial}{\partial c}\frac{\partial f^L(c_L)}{\partial c_L} = \frac{\partial c_L}{\partial c}\frac{\partial^2 f^L(c_L)}{\partial {c_L}^2}$

$$\psi^l{}_{cc} = \frac{f_{cc}^L(c_L)f_{cc}^S(c_S)}{[1 - q(Y, a)]f_{cc}^S(c_S) + q(Y, a)f_{cc}^L(c_L)} + \breve{q}(Y)\frac{d^2A^{S0}(\theta, c)}{dc^2}. \tag{28}$$

On the other hand, differentiating ${\psi^l}_c$ with respect to Y,

$$\begin{aligned} {\psi^l}_{cY} &= \frac{d}{dY}\left[\frac{df^L(c_L)}{dc_L}\right] + \frac{dA^{S0}(\theta,c)}{dc}\breve{q}'(Y) \\ &= \frac{d^2f^L(c_L)}{{dc_L}^2}\frac{\partial c_L}{\partial Y} + \frac{dA^{S0}(\theta,c)}{dc}\breve{q}'(Y) \\ &= \frac{(c_S^B - c_L^B)q'(Y,a)f_{cc}^S(c_S)f_{cc}^L(c_L)}{[1-q(Y,a)]f_{cc}^S(c_S)+q(Y,a)f_{cc}^L(c_L)} + \frac{dA^{S0}(\theta,c)}{dc}\breve{q}'(Y). \end{aligned} \tag{29}$$

The Cahn-Hilliard equation, governing the evolution of conserved variables,

$$c_t = \nabla.\frac{D(Y)}{{\psi^l}_{cc}}\nabla{\psi^l}_c. \tag{30}$$

Here, $D(Y)$ is the diffusivity. Substituting the value of ${\psi^l}_c$ from Equation (26),

$$\frac{\partial c}{\partial t} = \nabla\left[\frac{D(Y)}{{\psi^l}_{cc}}\nabla\left\{\frac{df^L(c_L)}{dc_L} + \breve{q}(Y)\frac{dA^{S0}(\theta,c)}{dc}\right\}\right]. \tag{31}$$

Equations (25) and (31) are the basic equations governing the transformation of binary alloys. We will consider simplified cases of technological importance in the next four subsections, i.e., Sections 2.1–2.5, which are included for completeness and can be omitted if numerical simulations of the model are of interest.

2.1. Dilute Solution Approximation

The dilute solution limit is frequently applicable to engineering problems and to study the fundamental physical mechanisms governing the phase transformation. Considering a binary alloy of A and B, the chemical potential of A and B can be approximated as [37],

$$\begin{aligned} &\mu_A^L = \mu_A^{oL} + R\theta ln(1-c);\ \ \mu_A^S = \mu_A^{oS} + R\theta ln(1-c); \\ &\mu_B^L = \mu_B^{oL} + R\theta ln(\gamma^L c);\ \ \mu_B^S = \mu_B^{oS} + R\theta ln(\gamma^S c). \end{aligned} \tag{32}$$

Here, R is the gas constant, and θ is the temperature of the isothermal system. γ^S and γ^L are the activity coefficients of solid and liquid phases, respectively. They are a measure of how much the thermodynamic characteristics of that mixture deviate from those of the ideal mixture. At equilibrium conditions, $\mu_A^L = \mu_A^S$ and $\mu_B^L = \mu_B^S$. Assuming liquid phase as a standard state,

$$\mu_A^{oL} = 0; \mu_B^{oL} = 0, \tag{33}$$

and applying this relation of the thermochemical potential at equilibrium concentration, we can rewrite Equation (32) as,

$$\begin{aligned} &\mu_A^L = \mu_A^S \Rightarrow \mu_A^{oL} + R\theta ln\left(1-c_L^e\right) = \mu_A^{oS} + R\theta ln\left(1-c_S^e\right) \\ &\Rightarrow \mu_A^{oS} = R\theta ln\left(\tfrac{1-c_L^e}{1-c_S^e}\right), \\ &\mu_B^L = \mu_B^S \Rightarrow \mu_B^{oL} + R\theta ln\left(\gamma^L c_L^e\right) = \mu_B^{oS} + R\theta ln\left(\gamma^S c_S^e\right) \\ &\Rightarrow \mu_B^{oS} = R\theta ln\left(\tfrac{c_L^e}{c_S^e}\right) + R\theta ln\left(\tfrac{\gamma^L}{\gamma^S}\right). \end{aligned} \tag{34}$$

Here, c_L^e and c_S^e, are the equilibrium concentration of the liquid side and solid side, respectively. We can set $\gamma^L = \gamma^S = 1$ as these values do not affect the equilibrium state and the driving force for the transformation. These relations are used to derive the free energy density of solid and liquid. We use the following form of the free energy density for the liquid phase [37],

$$\begin{aligned} &f^L(c_L) = \frac{\left[(1-c_L)\mu_A^{oL} + c_L\mu_B^{oL} + R\theta\{c_L ln(c_L) + (1-c_L)ln(1-c_L)\}\right]}{V_m}, \\ &\Rightarrow f^L(c_L) = \tfrac{R\theta}{V_m}[c_L lnc_L + (1-c_L)ln(1-c_L)]. \end{aligned} \tag{35}$$

Here, V_m is the molar volume. Differentiating Equation (35) with respect to c_L,

$$f^L_{c_L}(c_L) = \frac{R\theta}{V_m} ln\left(\frac{c_L}{1-c_L}\right). \tag{36}$$

Again, differentiating Equation (36) with respect to c_L,

$$f^L_{cc}(c_L) = \frac{R\theta}{V_m}\frac{1}{(1-c_L)c_L}. \tag{37}$$

The free energy density of the solid phase is [37],

$$\begin{array}{l} f^S(c_S) = \frac{\left[(1-c_S)\mu^{oS}_A + c_S\mu^{oS}_B + R\theta\{c_S lnc_S + (1-c_S)ln(1-c_S)\}\right]}{V_m}, \\ \Rightarrow f^S(c_S) = \frac{R\theta}{V_m}\left[(1-c_S)ln\left(\frac{1-c^e_L}{1-c^e_S}\right) + c_S ln\left(\frac{c^e_L}{c^e_S}\right) + c_S lnc_S + (1-c_S)ln(1-c_S)\right]. \end{array} \tag{38}$$

Differentiating Equation (38) with respect to c_S,

$$f^S_{c_S}(c_S) = \frac{R\theta}{V_m} ln\left(\frac{c_S}{1-c_S}\,\frac{1-c^e_L}{1-c^e_S}\,\frac{c^e_L}{c^e_S}\right). \tag{39}$$

Again differentiating Equation (40) with respect to c_S,

$$f^S_{cc}(c_S) = \frac{R\theta}{V_m}\frac{1}{(1-c_S)c_S} ln\left(\frac{1-c^e_L}{1-c^e_S}\,\frac{c^e_L}{c^e_S}\right). \tag{40}$$

Putting the value from Equations (36) and (39) in Equation (8) and reorganizing,

$$\frac{c^e_S c_L}{c^e_L c_S} = \frac{(1-c^e_S)(1-c_L)}{(1-c^e_L)(1-c_S)}. \tag{41}$$

Now,

$$G(c_S,\, c_L) \equiv\ \Delta G^{\theta}_{S0}(\theta, c) + \frac{df^L(c_L)}{dc_L}\left(c^B_S - c^B_L\right) = f^L(c_L) - f^S(c_S) - (c_L - c_S)f^L_{c_L}(c_L). \tag{42}$$

Substituting the value from Equations (35), (36) and (38),

$$G(c_S,\, c_L) = \frac{R\theta}{V_m} ln\frac{(1-c^e_S)(1-c^B_L)}{(1-c^e_L)(1-c^B_S)}. \tag{43}$$

Using Taylor's expansion and neglecting the higher-order terms,

$$G(c_S,\, c_L) = \frac{R\theta}{V_m}[(c^e_L - c^e_S) - (c_L - c_S)]. \tag{44}$$

At limit where all compositions go to zero Equation (41) can be approximated as

$$\frac{c_S}{c_L} = \frac{c^e_S}{c^e_L} = k^e, \tag{45}$$

where k^e is the equilibrium partition coefficient. Substituting $c_S = k^e c_L$ and $c^e_S = k^e c^e_L$ in Equation (44) we can derive,

$$G(c_S,\, c_L) = \frac{R\theta}{V_m}[(c^e_L - k^e c^e_L) - (c_L - k^e c_L)] = \frac{R\theta}{V_m}\frac{1-k^e}{m^e}(m^e c^e_L - m^e c_L), \tag{46}$$

Here, m^e is the liquids slope in the phase diagram. For the dilute solution [38],

$$\theta = \theta_m - m^e c_L \left(1 + \frac{(k^e - k) + kln\left(\frac{k}{k^e}\right)}{1 - k^e}\right) - \frac{V_m}{R\theta}\frac{\alpha m^e}{1 - k^e} V_n. \tag{47}$$

Here, V_n is the interface velocity, and $k = c_S/c_L$. For equilibrium condition, $k^e = k$, and interface velocity, $V_n = 0$. θ_m is the melting temperature of the pure solvent. So, Equation (47) reduces to,

$$\theta = \theta_m - m^e c_L^e. \tag{48}$$

From Equation (46),

$$G(c_S,\ c_L) = \frac{R\theta}{V_m}\frac{1 - k^e}{m^e}(\theta_m - \theta - m^e c_L). \tag{49}$$

Now from Equation (25),

$$\frac{1}{L_Y}\frac{\partial Y}{\partial t} = -\left\{q'(Y,a)G(c_S,\ c_L) + A^{S0}(\theta,c)\breve{q}'(Y)\right\} + \breve{q}(Y)\frac{\partial A^{S0}(\theta,c)}{\partial Y} + \nabla.\left[\beta^{S0}\nabla Y\right]. \tag{50}$$

Substituting the value from Equation (49),

$$\frac{1}{L_Y}\frac{\partial Y}{\partial t} = -\left\{q'(Y,a)\frac{R\theta}{V_m}\frac{1 - k^e}{m^e}(\theta_m - \theta - m^e c_L) + A^{S0}(\theta,c)\breve{q}'(Y)\right\} + \nabla.\left[\beta^{S0}\nabla Y\right]. \tag{51}$$

For a dilute solution, the height of double-well potential is constant. Putting the value of Equations (37) and (40), in Equation (28),

$$\psi^l{}_{cc} = \frac{R\theta}{V_m}\frac{1}{(1 - q(Y,a))(1 - c_L)c_L + q(Y,a)(1 - c_S)c_S}. \tag{52}$$

So,

$$H(Y,c_S,c_L) \equiv \frac{R\theta}{V_m\psi^l{}_{cc}} = (1 - q(Y,a))(1 - c_L)c_L + q(Y,a)(1 - c_S)c_S. \tag{53}$$

Now putting the value of Equations (36) and (53) in Equation (31),

$$\frac{\partial c}{\partial t} = \nabla\left[D(Y)H(Y,c_S,c_L)\nabla ln\left(\frac{c_L}{1 - c_L}\right)\right]. \tag{54}$$

In summary, we derived the kinetic GL equations for the dilute solution approximation, i.e., Equations (51) and (54), respectively.

2.2. Analytical Solution of Ginzburg-Landau Equation

From Equations (4), (5) and (7) the local free energy is,

$$\psi^l = G_0^\theta + \Delta G_{S0}^\theta(\theta,c)\left[aY^2 - 2(a-2)Y^3 + (a-3)Y^4\right] + A^{S0}(\theta,c)\left[Y^2(1-Y)^2\right]. \tag{55}$$

Reorganizing Equation (55), assuming $a = 0$ and $G_0^\theta = 0$, we have

$$\psi^l = A^{S0}(\theta,c)Y^2\left[1 - \frac{(6-P)Y}{3} + \frac{(4-P)Y^2}{4}\right], \tag{56}$$

where,

$$P(\theta,c) = \frac{12\Delta G_{S0}^\theta(\theta,c)}{A^{S0}(\theta,c)}. \tag{57}$$

Differentiating Equation (56) with respect to Y,

$$\frac{\partial \psi^l}{\partial Y} = A^{S0}(\theta, c)Y(1-Y)[2-(4-P)Y]. \tag{58}$$

Now we calculate the maxima,

$$\begin{array}{l} \frac{\partial^2 \psi^l(0)}{\partial Y^2} = A^{S0}(\theta, c);\ \frac{\partial^2 \psi^l(1)}{\partial Y^2} = 2A^{S0}(\theta, c)(2-P); \\ Y_3 = \frac{2}{4-p}; \psi_3^l = \frac{\partial^2 \psi^l(Y_3)}{\partial Y^2} = \frac{4}{3}\frac{A^{S0}(\theta,c)(3-P)}{(4-P)^3}, \end{array} \tag{59}$$

where, ψ^l is maximum at Y_3. The 1D time-dependent GL equation is,

$$\frac{\partial Y}{\partial t} = -\lambda \frac{\partial \psi}{\partial Y} = -\lambda \left(\frac{\partial \psi^l}{\partial Y} - 2\beta^{S0}\frac{\partial^2 Y}{\partial x^2} \right). \tag{60}$$

Here, $\lambda > 0$ is the kinetic coefficient. Now we rewrite Equation (60) in dimensionless form. The dimensionless potentials and order parameters are,

$$g = m\psi^l = B\xi^2 - \xi^3 + \xi^4, \xi = kY, \tag{61}$$

where,

$$B = \frac{9(4-P)}{4(6-P)^2}, k = \frac{3(4-P)}{4(6-P)},\ m = \frac{81(4-P)^3}{A^{S0}(\theta,c)(6-P)^4} = \frac{k^2 B}{A^{S0}(\theta,c)}, \tag{62}$$

Here, k can be determined using the condition $\frac{\partial g}{\partial \xi} = 0$. Now we define ξ_1 and ξ_2,

$$\begin{array}{l} g = \xi^2(\xi - \xi_1)(\xi - \xi_2), \\ \xi_1 = 0.5\left(1 - \sqrt{1-4B}\right), \\ \xi_2 = 0.5\left(1 + \sqrt{1-4B}\right). \end{array} \tag{63}$$

Introducing new spatial and time variables,

$$y = \frac{k}{\sqrt{\beta^{S0}m}}x = \sqrt{\frac{A^{S0}(\theta,c)}{\beta^{S0}B}}x = \frac{2}{3}\sqrt{\frac{A^{S0}(\theta,c)}{\beta^{S0}}}\frac{6-P}{\sqrt{4-P}}x, \quad z = \frac{\lambda k^2}{m}t. \tag{64}$$

We obtain the dimensionless form of the GL equation,

$$\frac{\partial \xi}{\partial z} = -\left(\frac{\partial g}{\partial \xi} - 2\frac{\partial^2 \xi}{\partial y^2} \right). \tag{65}$$

We only consider time-independent solution so, $\frac{\partial Y}{\partial z} = 0$. The resulting equation is

$$\frac{\partial g}{\partial \xi} = 2\frac{\partial^2 \xi}{\partial y^2}. \tag{66}$$

Equation (66) is the equation of motion of material point with a mass equal to 2 in the potential field. An energy integral read,

$$\frac{d\xi}{dy} = \sqrt{g - g_0}, \tag{67}$$

where, g_0 is an integral constant. At points $\frac{d\xi}{dy} = 0$, at the center of nucleus $g = g_0$. So,

$$g_{GL}^* = g_{GL} - g_o = g - g_0 + \left(\frac{d\xi}{dy}\right)^2 = 2(g - g_0). \tag{68}$$

Equation (66) has a periodic solution with n diffuse interfaces. The total energy per unit area of n diffuse interface is given by,

$$e := \int_{-l}^{l} g_{GL}^{*} dy = 2n \int_{-l}^{l} \sqrt{g - g_0} d\xi. \tag{69}$$

Here, $l := \sqrt{\frac{A^{S0}(\theta,c)}{\beta^{S0}B}} L$, $2L$ is the length of a parallelepiped in the x-direction. The energy e is finite even for an infinite slab. Imposing the boundary conditions at the end of the slab,

$$\frac{d\xi(-l)}{dy} = \frac{d\xi(l)}{dy} = 0, \tag{70}$$

$$g(-l) = g(l) = g_o. \tag{71}$$

Using Equations (61) and (67),

$$y(\xi) = \int \frac{d\xi}{\sqrt{(B\xi^2 - \xi^3 + \xi^4 - g_o)}}. \tag{72}$$

Now we consider $g(\infty) = g(-\infty) = 0$, we find $P = 0$, $B = \frac{1}{4}$, $\xi_1 = \xi_2 = \frac{1}{2}$. $g = \xi^2\left(\xi - \frac{1}{2}\right)^2$. The solution of Equation (15) is [39],

$$\xi(y) = \left[2 + \left(1 + e^{-\frac{y-y_o}{2}}\right)\right]^{-1}, \tag{73}$$

$$Y(x) = \left[1 + e^{-\sqrt{\frac{A^{S0}(\theta,c)}{\beta^{S0}}}(x-x_o)}\right]^{-1}. \tag{74}$$

The solution is symmetric around $x = x_o$. The interface energy is given by [39],

$$E = \left(\frac{4}{3}\right)\sqrt{\beta^{S0}\psi_3^l}; \tag{75}$$

The interface thickness is defined as [39],

$$\Delta = p\sqrt{\beta^{S0}/\psi_3^l};\ \ 2.411 \leq p \leq 2.667, \tag{76}$$

The relationships for the interface energy and width obtained here are vital for determining the free parameters of the model reproducing these experimentally measurable quantities.

Considering the free energy of liquid and solid as,

$$f^L(c_L) = y = 5(x-7)^4 + 30, \tag{77}$$

$$f^S(c_S) = y = 2(x-3)^4 + 10, \tag{78}$$

Figure 1 shows the free energy curves of solid and liquid by dotted black and solid red curves, respectively. TL is the common tangent line. Now let us consider $x_1 \equiv c_L$ and $x_2 \equiv c_S$. Within the interface region, the composition of free energy density is represented as,

$$\psi = f^S(c_S) + \left[f^L(c_L) - f^S(c_S)\right]q(Y) + A^{S0}(\theta,c)\breve{q}(Y). \tag{79}$$

Here,

$$q(Y) = 4Y^3 - 3Y^4; \breve{q}(Y) = Y^2(1-Y)^2\ ;\ Y = \frac{c - c_S}{c_L - c_S}. \tag{80}$$

Total energy, ψ is represented by the curve TE in Figure 1. The height of the double-well potential, $A^{S0}(\theta, c)$ is assumed to be constant. As the height goes to zero, the curve passes through the intersecting point of Equations (77) and (78).

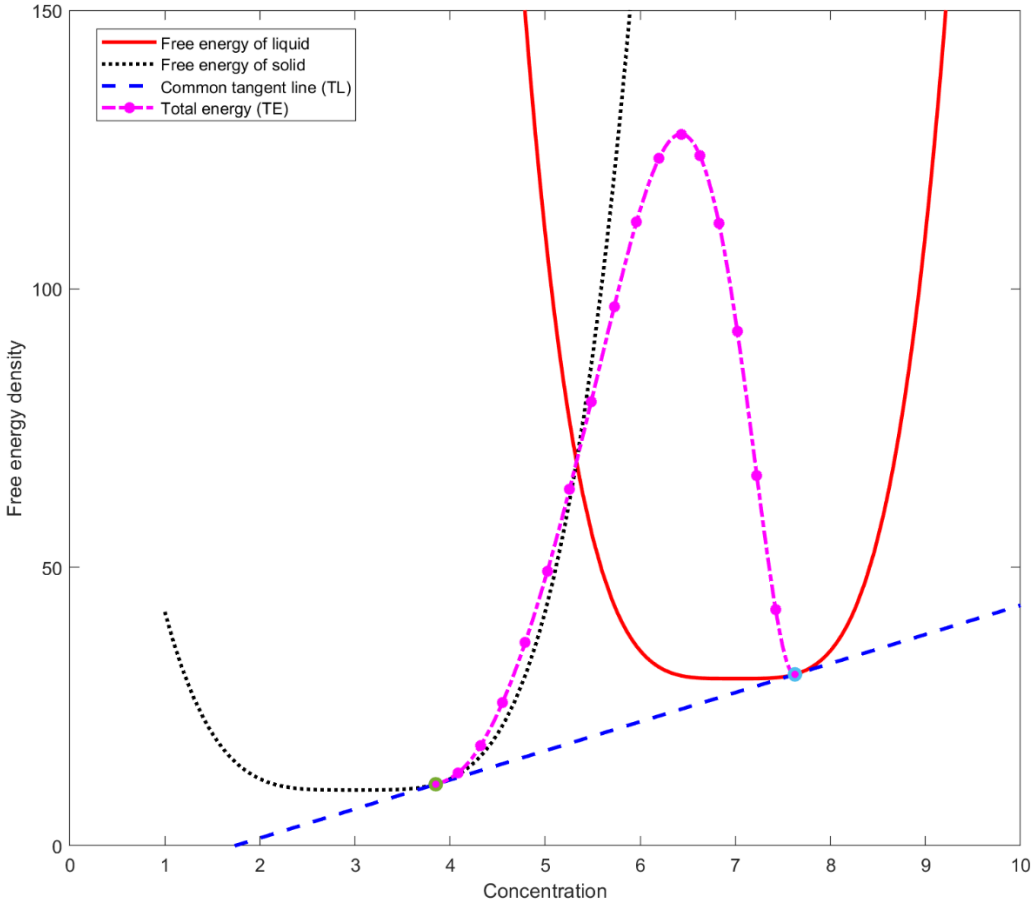

Figure 1. Free energy densities of solid and liquid vs. composition.

2.3. Thin Interface Limit

Equations (25) and (31) for the steady-state 1D problem, neglecting diffusivity in solid and assuming $A^{S0}(\theta, c)$ to be constant, for the thin interface limit, where the interface thickness is small compared to the diffusive boundary layer, become

$$-\frac{V}{L_Y}\frac{\partial Y}{\partial x} = -\left\{q'(Y,a)\left[\Delta G^{\theta}_{S0}(\theta,c) + \frac{df^L(c_L)}{dc_L}\left(c^B_S - c^B_L\right)\right] + A^{S0}(\theta,c)\breve{q}'(Y)\right\} + \beta^{S0}\frac{d^2Y}{dx^2}; \tag{81}$$

$$-V\frac{\partial c}{\partial x} = \frac{d}{dx}\left[\frac{D(Y)}{\psi^l{}_{cc}}\frac{d}{dx}\frac{df^L(c_L)}{dc_L}\right]. \tag{82}$$

where, V is the interface velocity. Integrating Equation (82),

$$Vc(x) + \frac{D(Y)}{\psi^l{}_{cc}}\frac{d}{dx}\frac{df^L(c_L)}{dc_L} = A, \tag{83}$$

A is an integration constant. On the liquid side, Equation (83) gives,

$$\begin{aligned} &\frac{D(Y)}{{\psi^l}_{cc}}\frac{d}{dx}\frac{df^L(c_L)}{dc_L} = A - Vc_L, \\ &\Rightarrow \frac{D(Y)}{{\psi^l}_{cc}}{\psi^l}_{cc}\frac{dc_L}{dx} = A - Vc_L, \\ &\Rightarrow D_L(Y)\frac{dc_L}{dx} = A - Vc_L. \end{aligned} \tag{84}$$

Similarly, for the solid side, we can derive that,

$$D_S(Y)\frac{dc_S}{dx} = A - Vc_S. \tag{85}$$

Assuming $D_S(Y)$ to be negligible,

$$A = Vc_S, \tag{86}$$

Putting the value of A in Equation (83) and integrating, we get the chemical potential profile [38],

$$f_c(x) = f_c^S(c_S) - V\int_{-\infty}^{x}\frac{{\psi^l}_{cc}}{D(Y)}[c(x) - c_S]dx, \tag{87}$$

Here, $f_c^S(c_S)$ is the integration constant, representing the chemical potential of the solid phase. To calculate the chemical potential of liquid, we assume that the thermodynamic partitioning of concentration at the interface occurs sufficiently over the width of $-\lambda < x < \lambda$. Thus, the chemical potential of liquid is

$$f_c^L(c_L) = f_c^S(c_S) - V\int_{-\lambda}^{\lambda}\frac{{\psi^l}_{cc}}{D(Y)}\left[c(x) - c_S^i\right]dx, \tag{88}$$

where c_S^i is the composition at the solid side $(x = -\lambda)$. The chemical potential's profile across the interface is given by,

$$f_c^L(c_L) = f_c^S\left(c_S^i\right) - V\int_{-\lambda}^{\lambda}\frac{{\psi^l}_{cc}}{D(Y)}\left[c(x) - c_S^i\right]dx, \tag{89}$$

For equilibrium condition,

$$\Delta G_{S0}^{\theta}(\theta, c) + f_c^L(c_L)\left(c_S^B - c_L^B\right) = \Delta G_{S0}^{\theta}(\theta, c^e) - (c_L^e - c_S^e)f_{c_L}^L(c_L), \tag{90}$$

$${\psi^l}_{cc} = {\psi^{le}}_{cc}, \tag{91}$$

Now multiplying Equation (81) with $\frac{dY}{dx}$ and integrating from $-\lambda$ to λ gives,

$$\begin{aligned} \tfrac{V}{L_Y}\textstyle\int_{-\lambda}^{\lambda}\left(\frac{dY}{dx}\right)^2 dx = &-\beta^{S0}\textstyle\int_{-\lambda}^{\lambda}\frac{d^2Y}{dx^2}\frac{dY}{dx}dx \\ &+\textstyle\int_{-\lambda}^{\lambda}\left(q'(Y,a)\left[\Delta G_{S0}^{\theta}(\theta, c^e) - \left(c_L^e - c_S^e\right)f_{c_L}^L(c_L)\right]\right)\frac{dY}{dx}dx \\ &+\textstyle\int_{-\lambda}^{\lambda}A^{S0}(\theta, c)\breve{q}'(Y)\frac{dY}{dx}dx. \end{aligned} \tag{92}$$

The first term of the right side of Equation (92),

$$-\beta^{S0}\int_{-\lambda}^{\lambda}\frac{d^2Y}{dx^2}\frac{dY}{dx}dx = \beta^{S0}\int_0^0\frac{dY}{dx}d\left(\frac{dY}{dx}\right) = 0. \tag{93}$$

The middle term of the right side of Equation (92),

$$\begin{aligned}&\int_{-\lambda}^{\lambda}\left(q'(Y,a)\left[\Delta G_{S0}^{\theta}(\theta,c^e)-\left(c_L^e-c_S^e\right)f_{c_L}^{L}(c_L)\right]\right)\frac{dY}{dx}dx\\&\quad=\int_1^0\left[\Delta G_{S0}^{\theta}(\theta,c^e)-\left(c_L^e-c_S^e\right)f_c^S\left(c_S^i\right)\right]q'(Y,a)dY\\&\quad-\int_1^0\left(c_L^e-c_S^e\right)\left[V\int_{-\lambda}^{\lambda}\frac{\psi^l{}_{cc}}{D(Y)}\left[c(x)-c_S^i\right]dx\right]q'(Y,a)dY.\end{aligned}\tag{94}$$

$$\begin{aligned}\Rightarrow&\int_{-\lambda}^{\lambda}\left(q'(Y,a)\left[\Delta G_{S0}^{\theta}(\theta,c^e)-\left(c_L^e-c_S^e\right)f_{c_L}^{L}(c_L)\right]\right)\frac{dY}{dx}dx\\&\quad=\Delta G_{S0}^{\theta}(\theta,c^e)-\left(c_L^e-c_S^e\right)f_c^S\left(c_S^i\right)\\&\quad-\int_1^0\left(c_L^e-c_S^e\right)\left[V\int_{-\lambda}^{\lambda}\frac{\psi^l{}_{cc}}{D(Y)}\left[c(x)-c_S^i\right]dx\right]q'(Y,a)dY,\end{aligned}$$

The third term of the right side of Equation (92),

$$\int_{-\lambda}^{\lambda}A^{S0}(\theta,c)\breve{q}'(Y)\frac{dY}{dx}dx=A^{S0}(\theta,c)\int_1^0\breve{q}'(Y)dY=0.\tag{95}$$

Putting these values from Equations (93)–(95) in (92),

$$\begin{aligned}\frac{V}{L_Y}\int_{-\lambda}^{\lambda}\left(\frac{dY}{dx}\right)^2dx&=\Delta G_{S0}^{\theta}(\theta,c^e)-\left(c_L^e-c_S^e\right)f_c^S\left(c_S^i\right)\\&\quad-\int_1^0\left(c_L^e-c_S^e\right)\left[V\int_{-\lambda}^{\lambda}\frac{\psi^l{}_{cc}}{D(Y)}\left[c(x)-c_S^i\right]dx\right]q'(Y,a)dY,\end{aligned}\tag{96}$$

From Equation (14) for equilibrium condition,

$$\frac{dc}{dY}=(c_S-c_L)q'(Y,a)\cong-(c_L^e-c_S^e)q'(Y,a).\tag{97}$$

So, Equation (96) can be rewritten as,

$$\begin{aligned}\frac{V}{L_Y}\int_{-\lambda}^{\lambda}\left(\frac{dY}{dx}\right)^2dx&=f^L(c_L^e)-f^S(c_S^e)-\left(c_L^e-c_S^e\right)f_c^S\left(c_S^i\right)\\&\quad+\int_{c_S}^{c_L}V\left[\int_{-\lambda}^{\lambda}\frac{\psi^l{}_{cc}}{D(Y)}\left[c(x)-c_S^i\right]dx\right]dc,\end{aligned}\tag{98}$$

From Equation (96) we can show that,

$$\Delta G_{S0}^{\theta}(\theta,c^e)-\left(c_L^e-c_S^e\right)f_c^S\left(c_S^i\right)=\alpha V,\tag{99}$$

where,

$$\alpha=\frac{1}{L_Y}\int_{-\lambda}^{\lambda}\left(\frac{dY}{dx}\right)^2dx+\int_1^0\left(c_L^e-c_S^e\right)\left[\int_{-\lambda}^{\lambda}\frac{\psi^l{}_{cc}}{D(Y)}\left[c(x)-c_S^i\right]dx\right]q'(Y,a)dY.\tag{100}$$

From common tangent relation in equilibrium,

$$f_{c_L}^{L}(c_L^e)=f_{c_S}^{S}(c_S^e)=\frac{f^L\left(c_L^e\right)-f^S\left(c_S^e\right)}{c_L^e-c_S^e}=\frac{\Delta G_{S0}^{\theta}(\theta,c^e)}{c_L^e-c_S^e}.\tag{101}$$

From Equation (99),

$$\left(c_L^e-c_S^e\right)\left[f_{c_S}^{S}(c_S^e)-f_c^S\left(c_S^i\right)\right]=\alpha V.\tag{102}$$

From dilute solution approximation,

$$f_{c_S}^S(c_S^e) - f_c^S\left(c_S^i\right) = \frac{R\theta}{v_m}\left(1 - \frac{c_S^i}{c_S^e}\right). \tag{103}$$

From Equations (102) and (103),

$$\begin{aligned}
&\left(c_L^e - c_S^e\right)\left[\tfrac{R\theta}{V_m}\left(1 - \tfrac{c_S^i}{c_S^e}\right)\right] = \alpha V\\
&\Rightarrow \left(c_L^e - c_S^e\right)\left(1 - \tfrac{c_S^i}{c_S^e}\right) = V\tfrac{V_m}{R\theta}\alpha\\
&\Rightarrow c_L^e - c_S^e - \tfrac{c_S^i}{c_S^e}.c_L^e + c_S^i = V\tfrac{V_m}{R\theta}\alpha\\
&\Rightarrow c_L^e(1-k^e) - \tfrac{c_S^i}{k^e}(1-k^e) = V\tfrac{V_m}{R\theta}\alpha\\
&\Rightarrow c_L^e m^e - m^e\tfrac{c_S^i}{k^e} = V\tfrac{V_m}{R\theta}\tfrac{\alpha m^e}{1-k^e}\\
&\Rightarrow \theta_m - \theta - m^e\tfrac{c_S^i}{k^e} = V\tfrac{V_m}{R\theta}\tfrac{\alpha m^e}{1-k^e}\\
&\Rightarrow \theta = \theta_m - m^e\tfrac{c_S^i}{k^e} - V\tfrac{V_m}{R\theta}\tfrac{\alpha m^e}{1-k^e}
\end{aligned}$$

$$\theta = \theta_m - m^e\frac{c_S^i}{k^e} - V\beta, \tag{104}$$

where $\beta = \frac{V_m}{R\theta}\frac{\alpha m^e}{1-k^e}$. Equation (104) is the relationship in the classical sharp interface model between the temperature and composition, proving thermodynamic consistency of the proposed phase-field model.

2.4. Solute Trapping

Solute trapping is known as the dependence of jump in concentration through the interface on the interface velocity. The chemical potential depends on the position across the moving interface. The equality of the chemical potential implies that there is no composition gradient across the interface. Solute trapping occurs when the chemical potential varies across the moving interface. We considered a steady-state 1D, Equation (82), dilute solution with constant diffusivity, D_i, in both interfacial region and liquid phase and negligible diffusivity in the solid. We have,

$$-V\frac{\partial c}{\partial x} = \frac{d}{dx}\left[\frac{D_i}{{\psi^l}_{cc}}\frac{d}{dx}\frac{df^L(c_L)}{dc_L}\right]. \tag{105}$$

Here, V is the interface velocity. Integrating Equation (105),

$$Vc(x) + \frac{D_i}{{\psi^l}_{cc}}\frac{d}{dx}\frac{df^L(c_L)}{dc_L} = A. \tag{106}$$

On the solid side of the interface from Equation (86),

$$A = Vc_S^i. \tag{107}$$

Putting the value of A in Equation (106),

$$\frac{d}{dx}\frac{df^L(c_L)}{dc_L} = -\frac{V}{D_i}\left(c - c_S^i\right){\psi^l}_{cc}. \tag{108}$$

Now,

$$\frac{d}{dx}\frac{df^L(c_L)}{dc_L} = \frac{d^2f^L(c_L)}{{dc_L}^2}\frac{dc_L}{dx} = f_{cc}^L(c_L)\frac{dc_L}{dx}. \tag{109}$$

Substituting the value from Equation (37),

$$\frac{d}{dx}\frac{df^L(c_L)}{dc_L} = \frac{RT}{V_m}\frac{1}{(1-c_L)c_L}\frac{dc_L}{dx}. \tag{110}$$

For dilute alloy, $(1-c_L) \to 1$ and $(1-c_S) \to 1$. So, from Equation (110),

$$\frac{d}{dx}\frac{df^L(c_L)}{dc_L} = \frac{RT}{V_m}\frac{1}{c_L}\frac{dc_L}{dx}. \tag{111}$$

Additionally, from Equation (47),

$$\frac{c_S(x)}{c_L(x)} = \frac{c_S^e}{c_L^e} = k^e. \tag{112}$$

Substituting this relation in Equation (6),

$$c(x) = [1-(1-k^e)q(Y,a)]c_L. \tag{113}$$

From Equations (27), (37) and (40),

$$\psi^l{}_{cc} = \frac{RT}{v_m}\frac{\frac{1}{(1-c_L)c_L}\frac{1}{(1-c_S)c_S}}{[1-q(Y,a)]\frac{1}{(1-c_S)c_S} + q(Y,a)\frac{1}{(1-c_L)c_L}}, \tag{114}$$

which reduces to,

$$\psi^l{}_{cc} = \frac{RT}{v_m[1-(1-k^e)q(Y,a)]c_L}. \tag{115}$$

Putting the values from Equations (111) and (115) in Equation (108),

$$\frac{RT}{V_m}\frac{1}{c_L}\frac{dc_L}{dx} = -\frac{V}{D_i}\left(c - c_S^i\right)\frac{RT}{v_m[1-(1-k^e)q(Y,a)]c_L}. \tag{116}$$

Putting the value of c from Equation (113) and simplifying Equation (116),

$$\frac{dc_L}{dx} + \frac{V}{D_i}c_L = \frac{V}{D_i}\frac{c_S^i}{[1-(1-k^e)q(Y,a)]}. \tag{117}$$

Equation (117) can be rewritten as,

$$y'(x) + ay(x) = \frac{ab}{1-(1-c)f(x)}, \tag{118}$$

where, $a = V/D_i$, $b = c_S^i$, $c = k^e$ and $q(Y,a) = f(x)$. The general solution of Equation (118) is

$$y(x) = ke^{-ax} + e^{-ax}\int_1^x \frac{abe^{ax'}}{1-(1-c)f(x')}dx'. \tag{119}$$

Putting the values of a, b, and c in Equation (119),

$$c_L(x) = ke^{-\frac{V}{D_i}x} + e^{-\frac{V}{D_i}x}\int_1^x \frac{\frac{V}{D_i}c_S^i e^{\frac{V}{D_i}x'}}{1-(1-k^e)q(x')}dx'. \tag{120}$$

Under the boundary condition $c_L = \frac{c_S}{k^e} = c_S^i/k^e$ at $x = -\lambda$, we have

$$c_L(x) = \frac{c_S^i}{k^e}e^{-\frac{V}{D_i}(x+\lambda)} + \frac{V}{D_i}c_S^i e^{-\frac{V}{D_i}x}\int_{-\lambda}^x \frac{e^{\frac{V}{D_i}x'}}{1-(1-k^e)q(x')}dx'. \tag{121}$$

Substituting in Equation (113),

$$c(x) = [1-(1-k^e)q(Y,a)]\left[\frac{c_S^i}{k^e}e^{-\frac{V}{D_i}(x+\lambda)} + \frac{V}{D_i}c_S^i e^{-\frac{V}{D_i}x}\int_{-\lambda}^{x}\frac{e^{\frac{V}{D_i}x'}}{1-(1-k^e)q(x')}dx'\right]. \quad (122)$$

This equation expresses the equilibrium partition coefficient as a function of interface velocity. Equilibrium partition coefficient k is defined as the ratio of composition of the solid side to the liquid side of the interface or composition of the solid side of the interface to the maximum composition across the interface [40]. Equation (122) can be rewritten in dimensionless form as,

$$\widetilde{c}(x) = [1-(1-k^e)q(Y,a)]\left[\frac{1}{k^e}e^{-P\widetilde{x}} + Pe^{-P(\widetilde{x}+\frac{1}{2})}\int_{-0.5}^{x}\frac{e^{P\widetilde{x}'}}{1-(1-k^e)q(Y)}d\widetilde{x}'\right], \quad (123)$$

where $\widetilde{x} = x/2\lambda$ and $\widetilde{c} = c/c_S^i$. Here, interface Péclet number, $P = 2\lambda V/D$, controls partition coefficient k. We adopted $\alpha = 2.94$ and $k^e = 0.8$ with which ϕ changes from 0.05 to 0.95 at $-\lambda < x < \lambda$.

Figure 2 shows, for small P values, the value of $\widetilde{c} = c_{\max}/c_S^i$ is close to equilibrium. With increasing P, the height of the concentration profile and thickness of the diffusive boundary layer decrease around the interface.

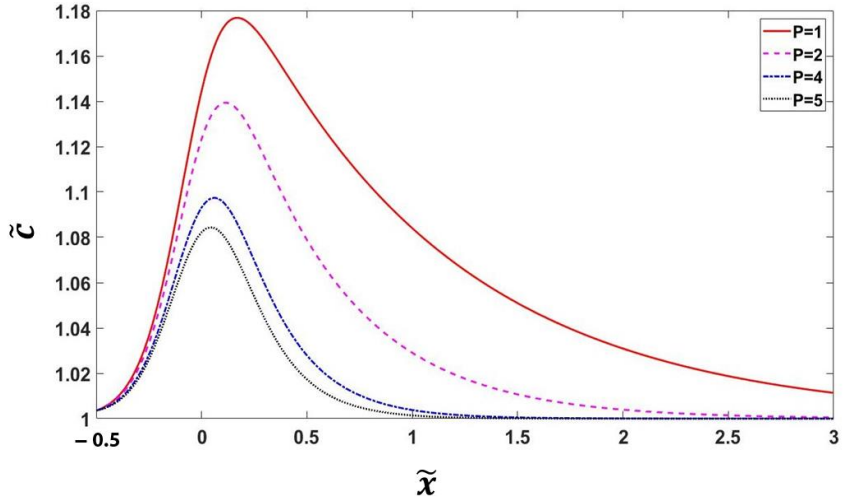

Figure 2. Variation of concentration profile for different Péclet numbers P.

Figure 3 shows the variation of partition coefficient, k, as a function of interface Péclet number P, indicating that the partition coefficient starts from 0.85 and gradually reaches 1 as P increases. From the definition, interface thickness can be defined as,

$$k(P) = \frac{k^e + \gamma P}{1+\gamma P}, \quad (124)$$

where,

$$\gamma = \frac{8(1-k^e)}{6\alpha \ln\left(\frac{1}{k^e}\right)}. \quad (125)$$

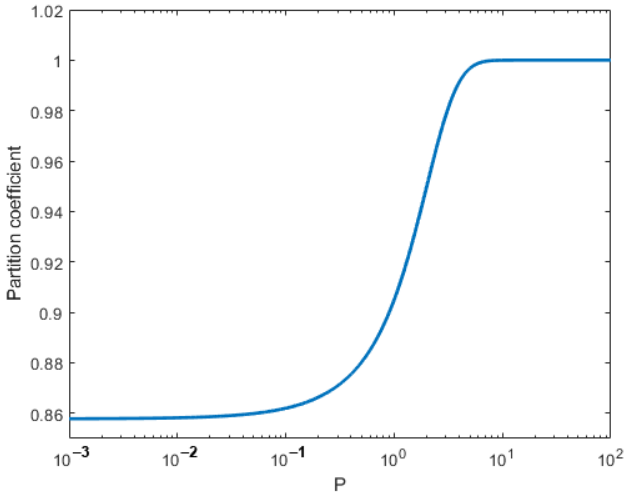

Figure 3. Variation of partition coefficient as a function of P.

Partitionless solidification occurs with complete solute trapping. The interface temperature θ is below θ_o temperature when $f^S(c_S)$ and $f^L(c_L)$ become equal. For dilute solution we have,

$$\theta < \theta_o = \theta_m + c_\infty \frac{m^e ln k^e}{1 - k^e}, \tag{126}$$

where c_∞ is the bulk composition. During partitionless solidification, the interface velocity is expressed as $(\theta_o - \theta)/\beta$ [41]. For dilute solution 1D phase-field equation from Equations (44), (46) and (81),

$$-\frac{V}{L_Y}\frac{\partial Y}{\partial x} = -\left\{q'(Y,a)\frac{R\theta}{V_m}[(c_L^e - c_S^e) - (c_L - c_S)] + A^{S0}(\theta,c)\breve{q}'(Y)\right\} + \beta^{S0}\frac{d^2Y}{dx^2}. \tag{127}$$

Additionally, for partitionless solidification, from Equation (113),

$$c_L = \frac{c_\infty}{[1 - (1 - k^e)q(Y,a)]}. \tag{128}$$

With approximation from Equation (112),

$$-\frac{V}{L_Y}\frac{V_m}{RT}\frac{\partial Y}{\partial x} = -\left\{q'(Y,a)c_L^e(1-k^e) - q'(Y,a)\frac{c_\infty(1-k^e)}{[1-(1-k^e)q(Y,a)]} + A^{S0}(\theta,c)\breve{q}'(Y)\right\} + \beta^{S0}\frac{d^2Y}{dx^2}. \tag{129}$$

Now,

$$\frac{d}{dY}ln[1-(1-k^e)q(Y,a)] = -q'(Y,a)\frac{(1-k^e)}{[1-(1-k^e)q(Y,a)]}. \tag{130}$$

Putting the value in Equation (129),

$$-\frac{V}{L_Y}\frac{V_m}{R\theta}\frac{\partial Y}{\partial x} = -\left\{q'(Y,a)c_L^e(1-k^e) + c_\infty\frac{d}{dY}ln[1-(1-k^e)q(Y,a)] + A^{S0}(\theta,c)\breve{q}'(Y)\right\} + \beta^{S0}\frac{d^2Y}{dx^2}. \tag{131}$$

Multiplying with $\frac{\partial Y}{\partial x}$ on both sides and integrate from $x = -\infty$ to $x = +\infty$,

$$\begin{aligned} &-\tfrac{V}{L_Y}\tfrac{V_m}{R\theta}\int_{-\infty}^{+\infty}\left(\tfrac{\partial Y}{\partial x}\right)^2 dx \\ &\quad = -\int_{-\infty}^{+\infty} q'(Y,a)c_L^e(1-k^e)\tfrac{\partial Y}{\partial x}dx \\ &\quad -\int_{-\infty}^{+\infty} c_\infty\tfrac{d}{dY}ln[1-(1-k^e)q(Y,a)]\tfrac{\partial Y}{\partial x}dx \\ &\quad -\int_{-\infty}^{+\infty} A^{S0}(\theta,c)\breve{q}'(Y)\tfrac{\partial Y}{\partial x}dx + \int_{-\infty}^{+\infty}\beta^{S0}\tfrac{d^2Y}{dx^2}\tfrac{\partial Y}{\partial x}dx. \end{aligned} \tag{132}$$

Similarly, from Equations (93) and (95),

$$\int_{-\infty}^{+\infty} A^{S0}(\theta, c)\breve{q}'(Y)\frac{\partial Y}{\partial x}dx = 0, \tag{133}$$

and,

$$\int_{-\infty}^{+\infty} \beta^{S0}\frac{d^2Y}{dx^2}\frac{\partial Y}{\partial x}dx = 0. \tag{134}$$

Now,

$$\int_{-\infty}^{+\infty} q'(Y,a)c_L^e(1-k^e)\frac{\partial Y}{\partial x}dx = \int_0^1 q'(Y,a)c_L^e(1-k^e)dY = c_L^e(1-k^e). \tag{135}$$

Additionally,

$$\int_{-\infty}^{+\infty} c_\infty\frac{d}{dY}ln[1-(1-k^e)q(Y,a)]\frac{\partial Y}{\partial x}dx = \int_0^1 c_\infty\frac{d}{dY}ln[1-(1-k^e)q(Y,a)]dY = c_\infty lnk^e. \tag{136}$$

Putting the values,

$$\frac{V}{L_Y}\frac{V_m}{RT}\int_{-\infty}^{+\infty}\left(\frac{\partial Y}{\partial x}\right)^2 dx = c_L^e(1-k^e) + c_\infty lnk^e, \tag{137}$$

Therefore, the condition for partitionless solidification is,

$$c_L^e(1-k^e) + c_\infty lnk^e > 0. \tag{138}$$

2.5. Equilibrium and Stability Conditions for the Homogenous Phase

From Equation (19) we get,

$$\psi^l{}_Y = q'(Y,a)\left[\Delta G_{S0}^\theta(\theta,c) + \frac{\partial f^L(c_L)}{\partial c_L}\left(c_S^B - c_L^B\right)\right] + A^{S0}(\theta,c)\breve{q}'(Y) + \breve{q}(Y)\frac{\partial A^{S0}(\theta,c)}{\partial c}\left(c_S^B - c_L^B\right)q'(Y,a). \tag{139}$$

For simplicity, let us assume $A^{S0}(\theta, c)$ is constant. So $\frac{\partial A^{S0}(\theta,c)}{\partial c} = 0$.

$$\psi^l{}_Y = q'(Y,a)\left[\Delta G_{S0}^\theta(\theta,c) + \frac{\partial f^L(c_L)}{\partial c_L}\left(c_S^B - c_L^B\right)\right] + A^{S0}(\theta,c)\breve{q}'(Y), \tag{140}$$

Differentiating Equation (140) with respect to Y we have,

$$\begin{aligned}\psi^l{}_{YY} = {} & q''(Y,a)\left[\Delta G_{S0}^\theta(\theta,c) + \tfrac{\partial f^L(c_L)}{\partial c_L}\left(c_S^B - c_L^B\right)\right] \\ & + q'(Y,a)\tfrac{\partial}{\partial Y}\left[\Delta G_{S0}^\theta(\theta,c) + \tfrac{\partial f^L(c_L)}{\partial c_L}\left(c_S^B - c_L^B\right)\right] \\ & + A^{S0}(\theta,c)\breve{q}''(Y)\end{aligned} \tag{141}$$

Assuming $a = 0$, we have,

$$\begin{aligned} q(Y) &= 4Y^3 - 3Y^4, \\ q'(Y) &= 12Y^2 - 12Y^3, \\ q''(Y) &= 24Y - 36Y^2. \end{aligned} \tag{142}$$

We calculate the values at $Y = 0$ and $Y = 1$,

$$\begin{aligned} q(Y=0) = 0; \quad q'(Y=0) = 0; \quad q''(Y=0) = 0, \\ q(Y=1) = 1; \quad q'(Y=1) = 0; \quad q''(Y=1) = -12. \end{aligned} \tag{143}$$

We also have,

$$\begin{aligned} \breve{q}(Y) &= Y^2(1-Y)^2, \\ \breve{q}'(Y) &= 2Y - 6Y^2 + 4Y^3, \\ \breve{q}''(Y) &= 2 - 12Y + 12Y^2. \end{aligned} \tag{144}$$

We calculate the values at $Y = 0$ and $Y = 1$,

$$\begin{aligned} &\breve{q}(Y=0) = 0; \quad \breve{q}'(Y=0) = 0; \quad \breve{q}''(Y=0) = 2, \\ &\breve{q}(Y=1) = 0; \quad \breve{q}'(Y=1) = 0; \quad \breve{q}''(Y=1) = 2. \end{aligned} \tag{145}$$

From Equation (141),

$$\left.\frac{\partial^2 \psi^l}{\partial Y^2}\right|_{(Y=0)} = 2A^{S0}(\theta, c); \tag{146}$$

$$\left.\frac{\partial^2 \psi^l}{\partial Y^2}\right|_{(Y=1)} = 2A^{S0}(\theta, c) - 12\left[\Delta G^{\theta}_{S0}(\theta, c) + \frac{\partial f^L(c_L)}{\partial c_L}\left(c_S^B - c_L^B\right)\right]. \tag{147}$$

Equations (146) and (147) give the value of $\frac{\partial^2 \psi^l}{\partial Y^2}$ at $Y = 0$ and $Y = 1$, respectively. At, $Y = 0$, for $M \to S$ phase transformation,

$$\begin{aligned} \frac{\partial^2 \psi^l}{\partial Y^2} &\leq 0, \\ A^{S0} &\leq 0. \end{aligned} \tag{148}$$

At $Y = 1$, for $S \to M$ phase transformation,

$$\begin{aligned} &\tfrac{\partial^2 \psi^l}{\partial Y^2} \leq 0; \\ &A^{S0} - 6\left[\Delta G^{\theta}_{S0}(\theta, c) + \tfrac{\partial f^L(c_L)}{\partial c_L}\left(c_S^B - c_L^B\right)\right] \leq 0. \end{aligned} \tag{149}$$

Now let $\Delta G^{\theta}_{S0}(\theta, c) = -\Delta S_{S0}\left(\theta - \theta_e^{S0}\right)$, here $\Delta S_{S0} < 0$ is the difference in entropy between the solid and liquid phases. θ_e^{S0} is the thermodynamic equilibrium melting temperature of the solid. $A^{S0} = A_c^{S0}\left(\theta - \theta_c^{S0}\right)$, where θ_c^{S0} is the critical temperature where liquid loses its stability.

2.6. Numerical Simulation

Let us consider a 1D isothermal system with uniform bulk modulus. The system temperature with undercooling is given. When the system temperature is lower than the solidus, the system can reach a steady state. The system can also reach a steady state when a solute sink exists and sweep over all solute influx from its neighbors. The classical sharp interface model with negligible diffusivity in solid can be described by [40],

$$-V\frac{dc}{dx} = D_L\frac{d^2c}{dx^2}, \tag{150}$$

$$V(1-k^e)c^i = -D_L\frac{dc}{dx}, \tag{151}$$

$$T = T_m - m^e c^i - \beta V, \tag{152}$$

$$c(\xi^*) = c_\infty. \tag{153}$$

Here, ξ^* is denoted as the distance between the solute sin k and the interface. c^i is the concentration at the interface. The exact solution of Equations (150)–(153) is,

$$c(x) = c_\infty + c_\infty \frac{(1-k^e)\left(e^{-\frac{Vx}{D_L}} - e^{-\frac{V\xi^*}{D_L}}\right)}{1-(1-k^e)\left(1-e^{-\frac{V\xi^*}{D_L}}\right)}, \tag{154}$$

Then, the interface velocity is determined by,

$$\beta V = T_m - T - \frac{m^e c_\infty}{1-(1-k^e)\left(1-e^{-\frac{V\xi^*}{D_L}}\right)}, \tag{155}$$

In Equation (155) $\xi^* \to \infty$ implies that interface velocity is positive if solidus temperature T_{Sol} is greater than temperature T, here $T_{Sol} = T_m - m^e c_\infty / k^e$. Additionally, when ξ^* has a finite value, the interface velocity is positive if the liquidus temperature is greater than the temperature T, here $T_{Liq} = T_m - m^e c_\infty$. Again, an exact solution for partitionless solidification is available. In this case, the interface velocity is given by,

$$V = \frac{T_0 - T}{\beta}, \tag{156}$$

T_0 is the temperature where the free energies of solid and liquid become equal. For computational work, we considered a diluted solution. Equations (9), (25) and (31) are used for our model with $q(Y) = 4Y^3 - 3Y^4$. The model system was chosen to be Ni-Cu (0.05 mole fraction alloy). The material parameters used for computation are as follows: $D_S = 1 \times 10^{-14}\mathrm{m}^2/\mathrm{s}$, $D_L = 1 \times 10^{-9}\mathrm{m}^2/\mathrm{s}$, $T_m = 1728.0$ K, $k^e = 0.7965$, $m^e = 310.9$, $T_{Sol} = 1708.5$ K, $T_{Liq} = 1712.5$ K, $\sigma = 0.37\ \mathrm{J/m}^2$, $\beta = 10$ Ks/m, the grid size was 1nm and between the interface the phase field vary from 0.05 to 0.95. From Equations (155), (152), (104) and (156) putting the value of T_{Sol} and Equation (126), the relations of interface velocity is expressed as,

$$\beta V = T_{Sol} - T, \tag{157}$$

$$\beta V = T_{Sol} - T + m^e\left(\frac{c_\infty}{k^e} - c^i\right), \tag{158}$$

$$\beta V = T_{Sol} - T + m^e c_\infty\left(\frac{1}{k^e} + \frac{lnk^e}{1-k^e}\right), \tag{159}$$

$$\beta V = T_{Sol} - T + \frac{m^e}{k^e}\left(c_\infty - c_S^i\right), \tag{160}$$

Here, Equation (157) is for analytical solution for classical sharp interface mode. Equation (158) is the sharp interface model with diffusion in liquid only. Equation (159) is the analytical solution for partitionless solidification, and Equation (160) is for the thin interface limit at low Péclet number conditions.

3. Results and Discussion

Figure 4 shows the variation of interface velocity as a function of undercooling $T_{Sol} - T$ ignoring the solute sink ($\xi^* \to \infty$). The solid straight line shows the analytical solution of Equation (155). The curved dashed line shows the analytical solution of partitionless solidification $V = (T_0 - T)/\beta$. The dotted line and the green line are calculated from the thin interface limit and sharp interface limit. For a thin interface, limit the interface velocity marge with an analytical solution as undercooling decreases. At large undercooling, the sharp interface limit's interface velocity is close to the analytical solution of partitionless solidification.

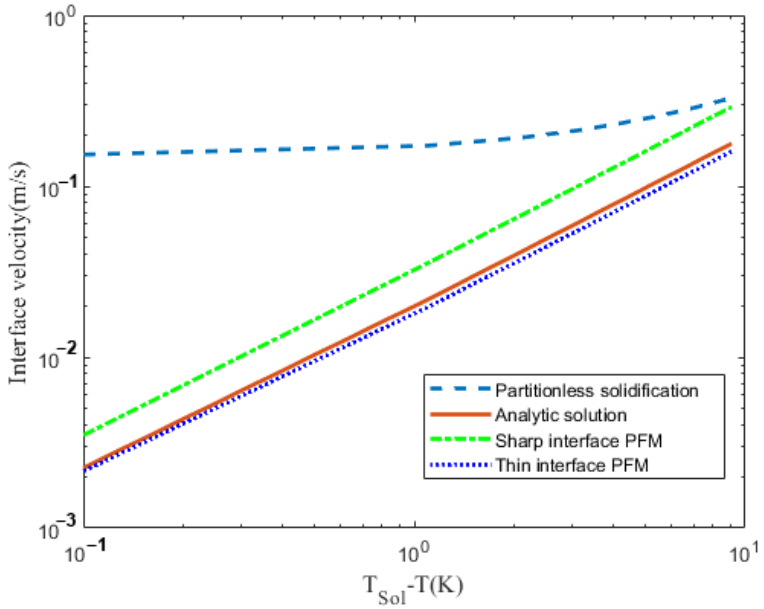

Figure 4. Variation of interface velocity, calculated at $\xi^* \to \infty$ as a function of $T_{Sol} - T$.

Figure 5 shows the variation of interface velocity as a function of the distance between interface and solute sink $,^*$ in liquid neglecting the kinetic coefficient. The system temperature was 1709 K. The curved line shows the analytical solution of Equation (155). The physical meaning of zero kinetic coefficients in thin interface alloy means a decrease of solid composition by phase-field alloy or increase of the solid composition by interface thickness, bringing the solute trapping effect increases the solid composition.

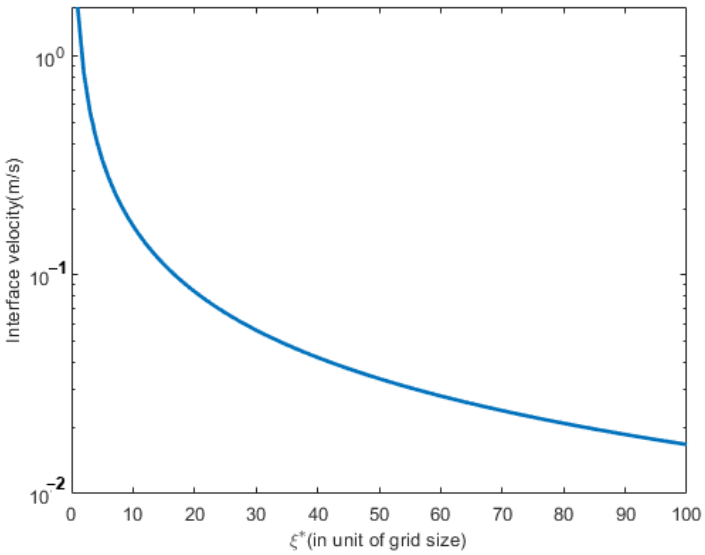

Figure 5. Variation of interface velocity calculated neglecting kinetic effect as a function of ξ^*.

Figure 6 shows the variation in solid composition along with the interface for $Y < 0.5$. The vertical axis represents the relative difference between the measured solid composition at the interface c_S^i and the equilibrium composition c_S^e, scaled by the equilibrium composition c_S^e. Figure 7a show the change in variation of solid composition with a coefficient of phase-field gradient energy, β^{S0} along with the interface for $D^* = 1$. Figure 7b shows the change in Y with a coefficient of phase-field gradient energy along with the interface for $D^* = 1$. We did not detect any difference in Deviation of solid composition and Y profile for different D^* values. From the plot, we can see that as the coefficient of gradient energy decreases, the phase-field model approaches the sharp interface limit.

Figure 8a,b show the deviation of solid composition at the interface with diffusivity: $D^* = 1, D^* = 2$ and $D^* = 5$ for $\beta^{S0} = 1$ and $\beta^{S0} = 2$, respectively. From the figure, we can say that diffusivity has no effect on solid composition in the interface region.

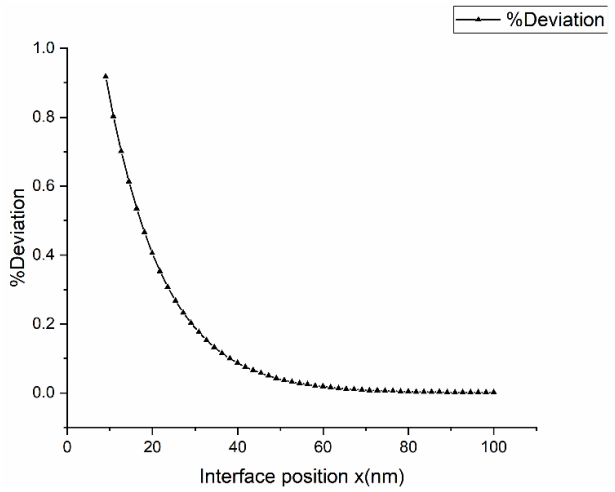

Figure 6. Variation of solid composition along with the interface.

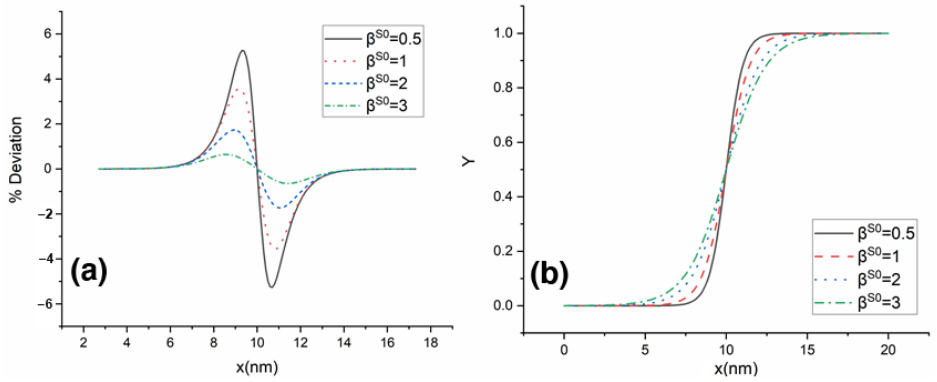

Figure 7. Deviation of solid composition (**a**) and Y profile (**b**) along the interface for dimensionless diffusivity $D^* = 1$ for various β^{S0} values.

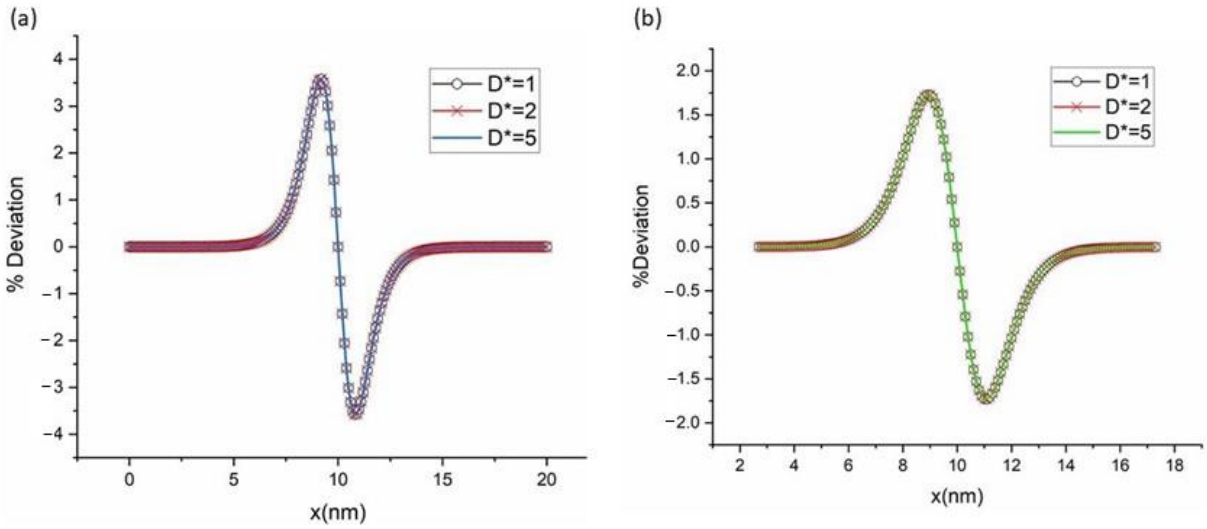

Figure 8. Deviation of solid composition along with the interface with dimensionless diffusivity $D^* = 1, D^* = 2$, and $D^* = 5$ for (**a**) $\beta^{S0} = 1$; (**b**) $\beta^{S0} = 2$.

For the validation of our simulation with the analytical result, we use the analytical solution of GL equation Equation (74) and simulation result of Y with the same material properties. Figure 9 shows that the analytical solution coincides with the simulation result. So, the simulation results are in excellent agreement with the analytical solution, indicating the current implementation of the finite element code.

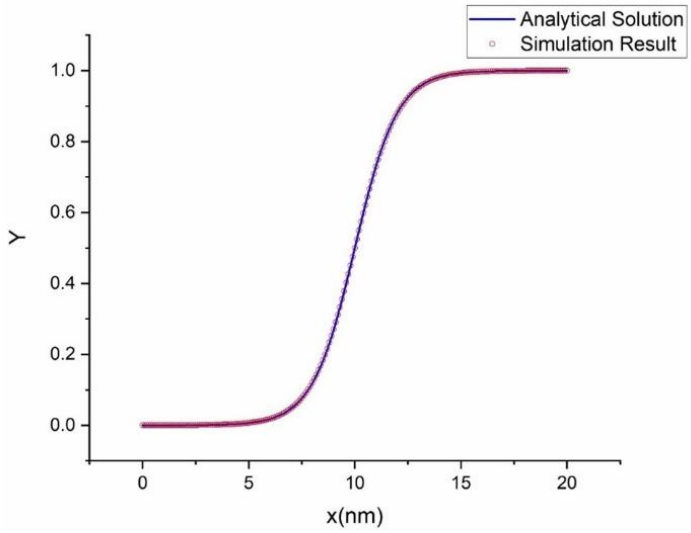

Figure 9. Comparison of numerical result with the analytical result. Our finite element code reproduces matches with the analytical solution.

4. Conclusions

We developed a phase-field model for the solidification of binary alloys, which satisfies the stability conditions at all temperatures. The proposed phase-field potential is composed of local and gradient energy terms, and we derived the GL equations governing the solidification kinetics using the second law of thermodynamics followed by the Onsager assumption. The phase-field model was reformulated for the dilute approximation limit and solved analytically for the 1D problem. We also demonstrate that the proposed phase-field model reduced to the sharp-interface solution at the thin interface limit.

We developed the relationship between kinetic coefficient and mobility for thin-interface limit, neglecting diffusivity in the solid phase. Our results indicate that the solid composition increases with the effect of finite interface thickness and decreases with finite phase-field mobility. With a zero kinetic coefficient, both these effects are canceled out that results in equilibrium at the interface.

Using this model for 1D steady-state dilute solution with negligible diffusivity, we observed the concentration profile as a function of Péclet number, which is a function of interface velocity. From the analytical solution, it is concluded that with increasing interface velocity, the concentration profile decreases. The distribution of the partition coefficient was also obtained. From the relation between interface velocity and partition coefficient, we can see that with high interface velocity, the value of partition coefficient goes close to unity for sharp interface model. For 1D dilute solution, we performed numerical simulations. From simulation results, we can conclude that the concentration profile's height is inversely proportional to the coefficient of gradient energy.

Author Contributions: K.M.: Supervision, Project administration; J.R.: Writing—Review and Editing; M.G.: Methodology, Data Curation, Writing—Original draft; M.H.: Writing—Review and Editing. All authors have read and agreed to the published version of the manuscript.

Funding: The authors want to acknowledge the support from DoE-ARPA-E OPEN (DE-AR0001066), National Aeronautics and Space Administration (NASA)'s Established Program to Stimulate Competitive Research (EPSCoR) Cooperative Agreement number 80NSSC19M0149, the University of Alabama, and the NSF-CAREER under NSF cooperative agreement CBET-2042683.

Institutional Review Board Statement: Not applicable.

Informed Consent Statement: Not applicable.

Data Availability Statement: Data will be provided upon request.

Conflicts of Interest: The authors declare no conflict of interest.

References

1. Clinton, R.G. Overview of Additive Manufacturing Initiatives at NASA Marshall Space Flight Center—In Space and Rocket Engines. Available online: https://ntrs.nasa.gov/api/citations/20170001772/downloads/20170001772.pdf (accessed on 28 November 2022).
2. Cahn, J.W.; Hilliard, J.E. Spinodal Decomposition: A Reprise. *Acta Metall.* **1971**, *19*, 151–161. [CrossRef]
3. Cahn, J.W.; Hilliard, J.E. Free Energy of a Nonuniform System. I. Interfacial Free Energy. *J. Chem. Phys.* **1958**, *28*, 258–267. [CrossRef]
4. Cahn, J.W.; Allen, S.M. A Microscopic Theory for Domain Wall Motion and Its Experimental Verification in Fe-Al Alloy Domain Growth Kinetics. *J. Phys. Colloq.* **1977**, *38*, C7–C51. [CrossRef]
5. Wheeler, A.A.; Boettinger, W.J.; McFadden, G.B. Phase-Field Model for Isothermal Phase Transitions in Binary Alloys. *Phys. Rev. A* **1992**, *45*, 7424. [CrossRef] [PubMed]
6. Wheeler, A.A.; Boettinger, W.J.; McFadden, G.B. Phase-Field Model of Solute Trapping during Solidification. *Phys. Rev. E* **1993**, *47*, 1893. [CrossRef]
7. Glasner, K. Solute Trapping and the Non-Equilibrium Phase Diagram for Solidification of Binary Alloys. *Phys. D Nonlinear Phenom.* **2001**, *151*, 253–270. [CrossRef]
8. Bi, Z.; Sekerka, R.F. Phase-Field Model of Solidification of a Binary Alloy. *Phys. A Stat. Mech. Its Appl.* **1998**, *261*, 95–106. [CrossRef]
9. Loginova, I.; Amberg, G.; Ågren, J. Phase-Field Simulations of Non-Isothermal Binary Alloy Solidification. *Acta Mater.* **2001**, *49*, 573–581. [CrossRef]
10. Ramirez, J.C.; Beckermann, C. Examination of Binary Alloy Free Dendritic Growth Theories with a Phase-Field Model. *Acta Mater.* **2005**, *53*, 1721–1736. [CrossRef]
11. Ramirez, J.C.; Beckermann, C.; Karma, A.; Diepers, H.-J. Phase-Field Modeling of Binary Alloy Solidification with Coupled Heat and Solute Diffusion. *Phys. Rev. E* **2004**, *69*, 051607. [CrossRef]
12. Momeni, K.; Levitas, V.I. Propagating Phase Interface with Intermediate Interfacial Phase: Phase Field Approach. *Phys. Rev. B* **2014**, *89*, 184102. [CrossRef]
13. Levitas, V.I.; Preston, D.L.; Lee, D.-W. Three-dimensional Landau theory for multivariant stress-induced martensitic phase transformations. II. Multivariant phase transformations and stress space analysis. *Phys. Rev. B* **2002**, *66*, 134207. [CrossRef]
14. Momeni, K.; Levitas, V.I. A Phase-Field Approach to Solid–Solid Phase Transformations via Intermediate Interfacial Phases under Stress Tensor. *Int. J. Solids Struct.* **2015**, *71*, 39–56. [CrossRef]
15. Momeni, K.; Levitas, V.I.; Warren, J.A. The Strong Influence of Internal Stresses on the Nucleation of a Nanosized, Deeply Undercooled Melt at a Solid–Solid Phase Interface. *Nano Lett.* **2015**, *15*, 2298–2303. [CrossRef]
16. Momeni, K.; Levitas, V.I. A Phase-Field Approach to Nonequilibrium Phase Transformations in Elastic Solids via an Intermediate Phase (Melt) Allowing for Interface Stresses. *Phys. Chem. Chem. Phys.* **2016**, *18*, 12183–12203. [CrossRef]
17. Kumara, C.; Segerstark, A.; Hanning, F.; Dixit, N.; Joshi, S.; Moverare, J.; Nylén, P. Microstructure Modelling of Laser Metal Powder Directed Energy Deposition of Alloy 718. *Addit. Manuf.* **2019**, *25*, 357–364. [CrossRef]
18. Kavousi, S.; Novak, B.R.; Moldovan, D.; Asle Zaeem, M. Quantitative Prediction of Rapid Solidification by Integrated Atomistic and Phase-Field Modeling. *Acta Mater.* **2021**, *211*, 116885. [CrossRef]
19. Karayagiz, K.; Johnson, L.; Seede, R.; Attari, V.; Zhang, B.; Huang, X.; Ghosh, S.; Duong, T.; Karaman, I.; Elwany, A.; et al. Finite Interface Dissipation Phase Field Modeling of Ni–Nb under Additive Manufacturing Conditions. *Acta Mater.* **2020**, *185*, 320–339. [CrossRef]
20. Gu, Y.; He, X.; Han, D. On the Phase-Field Modeling of Rapid Solidification. *Comput. Mater. Sci.* **2021**, *199*, 110812. [CrossRef]
21. Zhang, L.; Danilova, E.V.; Steinbach, I.; Medvedev, D.; Galenko, P.K. Diffuse-Interface Modeling of Solute Trapping in Rapid Solidification: Predictions of the Hyperbolic Phase-Field Model and Parabolic Model with Finite Interface Dissipation. *Acta Mater.* **2013**, *61*, 4155–4168. [CrossRef]
22. Kavousi, S.; Zaeem, M.A. Quantitative Phase-Field Modeling of Solute Trapping in Rapid Solidification. *Acta Mater.* **2021**, *205*, 116562. [CrossRef]
23. Pinomaa, T.; Provatas, N. Quantitative Phase Field Modeling of Solute Trapping and Continuous Growth Kinetics in Quasi-Rapid Solidification. *Acta Mater.* **2019**, *168*, 167–177. [CrossRef]

24. Aziz, M.J.; Boettinger, W.J. On the Transition from Short-Range Diffusion-Limited to Collision-Limited Growth in Alloy Solidification. *Acta Metall. Et Mater.* **1994**, *42*, 527–537. [CrossRef]
25. Momeni, K. Sensitivity of Laser Powder Bed Fusion Additive Manufactured HAYNES230 to Composition and Print Parameters. *J. Mater. Res. Technol.* **2021**, *15*, 6453–6463. [CrossRef]
26. Momeni, K. Sensitivity of Additively Manufactured AA7075 to Variation in Feedstock Composition and Print Parameters. *J. Manuf. Process.* **2022**, *73*, 555–562. [CrossRef]
27. Ghosh, S. Predictive Modeling of Solidification during Laser Additive Manufacturing of Nickel Superalloys: Recent Developments, Future Directions. *Mater. Res. Express* **2018**, *5*, 012001. [CrossRef]
28. Bayat, M.; Dong, W.; Thorborg, J.; To, A.C.; Hattel, J.H. A Review of Multi-Scale and Multi-Physics Simulations of Metal Additive Manufacturing Processes with Focus on Modeling Strategies. *Addit. Manuf.* **2021**, *47*, 102278. [CrossRef]
29. Sahoo, S.; Chou, K. Review on Phase-Field Modeling of Microstructure Evolutions: Application to Electron Beam Additive Manufacturing. In *Proceedings of the International Manufacturing Science and Engineering Conference Volume 2, 9–13 June 2014*; American Society of Mechanical Engineers: Detroit, MI, USA, 2014.
30. Ji, Y.; Chen, L.; Chen, L.-Q. Understanding Microstructure Evolution during Additive Manufacturing of Metallic Alloys Using Phase-Field Modeling. In *Thermo-Mechanical Modeling of Additive Manufacturing*; Elsevier: Amsterdam, The Netherlands, 2018; pp. 93–116, ISBN 978-0-12-811820-7.
31. Li, J.; Zhou, X.; Brochu, M.; Provatas, N.; Zhao, Y.F. Solidification Microstructure Simulation of Ti-6Al-4V in Metal Additive Manufacturing: A Review. *Addit. Manuf.* **2020**, *31*, 100989. [CrossRef]
32. Gunasegaram, D.R.; Steinbach, I. Modelling of Microstructure Formation in Metal Additive Manufacturing: Recent Progress, Research Gaps and Perspectives. *Metals* **2021**, *11*, 1425. [CrossRef]
33. Levitas, V.I.; Momeni, K. Solid–Solid Transformations via Nanoscale Intermediate Interfacial Phase: Multiple Structures, Scale and Mechanics Effects. *Acta Mater.* **2014**, *65*, 125–132. [CrossRef]
34. Momeni, K.; Ji, Y.; Nayir, N.; Sakib, N.; Zhu, H.; Paul, S.; Choudhury, T.H.; Neshani, S.; van Duin, A.C.T.; Redwing, J.M.; et al. A Computational Framework for Guiding the MOCVD-Growth of Wafer-Scale 2D Materials. *npj Comput. Mater.* **2022**, *8*, 240. [CrossRef]
35. Momeni, K.; Ji, Y.; Chen, L.-Q. Computational Synthesis of 2D Materials Grown by Chemical Vapor Deposition. *J. Mater. Res.* **2022**, *37*, 114–123. [CrossRef]
36. Momeni, K.; Neshani, S.; Uba, C.; Ding, H.; Raush, J.; Guo, S. Engineering the Surface Melt for In-Space Manufacturing of Aluminum Parts. *J. Mater. Eng. Perform.* **2022**, *31*, 6092–6100. [CrossRef]
37. Lee, J.S.; Kim, S.G.; Kim, W.T.; Suzuki, T. Numerical Simulation of Peritectic Reaction Using a Multi-Phase-Field Model. *ISIJ Int.* **1999**, *39*, 730–736. [CrossRef]
38. Kim, S.G.; Kim, W.T.; Suzuki, T. Interfacial Compositions of Solid and Liquid in a Phase-Field Model with Finite Interface Thickness for Isothermal Solidification in Binary Alloys. *Phys. Rev. E* **1998**, *58*, 3316–3323. [CrossRef]
39. Levitas, V.I.; Preston, D.L.; Lee, D.-W. Three-Dimensional Landau Theory for Multivariant Stress-Induced Martensitic Phase Transformations. III. Alternative Potentials, Critical Nuclei, Kink Solutions, and Dislocation Theory. *Phys. Rev. B* **2003**, *68*, 134201. [CrossRef]
40. Kim, S.G.; Kim, W.T.; Suzuki, T. Phase-Field Model for Binary Alloys. *Phys. Rev. E* **1999**, *60*, 7186–7197. [CrossRef]
41. Ahmad, N.A.; Wheeler, A.A.; Boettinger, W.J.; McFadden, G.B. Solute Trapping and Solute Drag in a Phase-Field Model of Rapid Solidification. *Phys. Rev. E* **1998**, *58*, 3436–3450. [CrossRef]